Icarus 226 (2013) 77–88

Contents lists available at SciVerse ScienceDirect

Icarus

journal homepage: www.elsevier.com/locate/icarus

Temperature and variability of Pillan, Wayland Patera, and Loki Patera on Io from Cassini ISS data

Daniel R. Allen [a,*], Jani Radebaugh [b], Denise C. Stephens [a]

[a] Brigham Young University, Department of Physics and Astronomy, Provo, UT 84602, USA
[b] Brigham Young University, Department of Geological Sciences, Provo, UT 84602, USA

ARTICLE INFO

Article history:
Received 1 October 2012
Revised 16 May 2013
Accepted 21 May 2013
Available online 2 June 2013

Keywords:
Jupiter, Satellites
Io
Volcanism
Satellites, Surfaces

ABSTRACT

Cassini spacecraft images of Io obtained during its flyby of Jupiter in late 2000 and early 2001 were used to determine the lava composition and eruption style of three faint hot spots, Pillan, Wayland Patera, and Loki Patera. We found a maximum color temperature of 1130 ± 289 K for Pillan and maximum color temperatures of 1297 ± 289 K and 1387 ± 287 K for Wayland Patera and Loki Patera, respectively. These temperatures are suggestive of basaltic lava but an ultramafic composition cannot be ruled out. The temperatures with the best signal-to-noise ratios also suggested basaltic lava and were found to be 780 ± 189 K, 1116 ± 250 K, and 1017 ± 177 K for Pillan, Wayland Patera, and Loki Patera, respectively. Pillan showed constant thermal output within error over three days of observations. The data also suggest Pillan may be surrounded by topography that blocked emission in the middle of the observation and caused a more dramatic decrease in emission. Wayland Patera's intensity decreased over the three eclipse observations, consistent with a cooling lava flow or decreasing effusion rate. Intensities at Loki Patera over the course of the observations varied, consistent with previous determinations that Loki Patera is an often quiescent lava lake with periods of overturning, fountaining, and crustal foundering.

1. Introduction

The surface of Jupiter's moon Io is covered with volcanoes that result from the release of heat from the interior of the tidally heated moon (Peale et al., 1979). Studies of Io's thermal behavior lead to a better understanding of the elevated volcanic activity of the early Earth (Matson et al., 1998; Vlaar et al., 1994) and provide insights into heat dissipation on tidally heated bodies. Since lavas emit radiation at temperatures characteristic of their composition, determination of lava temperatures can lead to an understanding of the composition of Io's magmas and the dynamics and structure of the interior.

Io shows examples of both explosive and effusive eruptions as well as evidence of lavas of various compositions. Images of the surface reveal explosive eruptions in the form of large volcanic plumes of sulfur (S_2) (Spencer et al., 2000) and sulfur dioxide (Pearl et al., 1979), which create colorful deposits that surround many volcanoes. Mafic pyroclastic eruptions form dark diffuse deposits around volcanic centers (Williams et al., 2002). Images also show evidence of effusive eruptions in the form of large compound flows and lava lakes. Temperatures derived from ground-based and spacecraft observations of Io indicate silicate lava with compositions ranging from basaltic to ultramafic (e.g., Davies et al., 2001; Marchis et al., 2002; McEwen et al., 1998b; Radebaugh et al., 2004; Spencer et al., 1997, 2007). The question remains whether the majority of Io's lavas are basaltic or ultramafic. Although the volcanism is primarily silicate in nature, sulfur and sulfur dioxide still a play a role in the formation of plumes and frost on the surface that may produce secondary lava flows (Williams et al., 2001).

Of particular interest to us is the observational history of the three hot spots central to this study: Pillan, Wayland Patera, and Loki Patera. In 1997, the area around Pillan experienced a large eruption which initially covered 3100 km^2 of Io's surface. Additional lava flows flooded Pillan Patera (12°S, 242°W) and covered another 2500 km^2 for a total lava emplacement of 5600 km^2 (Keszthelyi et al., 2001). Galileo NIMS charted the eruption and subsequent cooling of these large flows (Davies et al., 2001). Temperatures measured by Galileo for Pillan have been among the highest measured for any hot spot on Io. McEwen et al. (1998b) reported brightness temperatures of 1500–1800 K, and Davies et al. (2001) quoted a temperature of 1870 K during the 1997 eruption at Pillan. Later work by Keszthelyi et al. (2007) suggested that these temperatures should be lowered by ~260 K, placing the temperatures within the basaltic regime. This study measures the temperature and variations in emission and temperature of an area in the 1997 flows to the north and east of Pillan

* Corresponding author. Present address: University of Wyoming, Department of Geology and Geophysics, Laramie, WY 82071, USA.
E-mail address: dallen7@uwyo.edu (D.R. Allen).

0019-1035/$ - see front matter © 2013 Elsevier Inc. All rights reserved.
http://dx.doi.org/10.1016/j.icarus.2013.05.026

Patera at approximately 11°S, 241°W as noted by Geissler et al. (2004).

Wayland Patera (33°S, 225°W), a circular feature measuring about 95 km across (Fig. 1), was detected as a faint hot spot by both Galileo NIMS and Galileo PPR in 2001 (Lopes et al., 2001; Rathbun et al., 2004). Rathbun et al. (2004) reported a temperature of 110 K for the area around and including Wayland Patera in nighttime temperature maps from PPR. Geissler et al. (2004) also identified Wayland Patera as a hot spot in Cassini ISS images, which implies an effective temperature of at least 700 K. The dark lava flows on the floor of Wayland Patera cover an area of 256 km^2 and indicate recent volcanic activity (Veeder et al., 2011). Veeder et al. (2011) used this area to derive an effective temperature of 242 K.

Loki Patera (13°N, 309°W) has been studied extensively through ground-based observations and analysis of Galileo data. Loki Patera measures about 200 km in diameter and contributes about 13% of the heat flow observed from Io (Spencer et al., 2002). Data suggest that Loki Patera is a large, relatively quiescent lava lake or magma sea which experiences periodic overturn of a cooling lava crust (Rathbun et al., 2002; Matson et al., 2006). Recent results by Davies et al. (2012) reinforce this idea by analyzing Galileo NIMS data at wavelengths around 5 μm. Typically, temperatures have been less than 1000 K and generally reside around 400–700 K (e.g., Davies, 2003; Howell and Lopes, 2007; McEwen et al., 1998a; Rathbun et al., 2002). Lower temperatures are not unexpected given the large expanses of cooling lava crusts found at Loki Patera that tend to overwhelm the signal from any small, high temperature areas. Many of these previous temperature values were also found using longer wavelength data, which are more sensitive to cooler surfaces. However, Blaney et al. (1995) found a value of 1225 K from ground-based observations of an outburst in January 1990 in the Loki Patera region and Matson et al. (2006) reported a high temperature of 990 K for two-temperature fits to Galileo NIMS data. Davies (1996, 2003) also suggested that higher temperatures (1100–1470 K) for Loki Patera are possible if emission from deep in the cracks on the surface of the lava is observed.

For this study, we analyzed images of Io taken by the Cassini spacecraft as it passed through the Jupiter system on its way to Saturn. Cassini collected nearly 500 images of Io in late 2000 and early 2001 over a wavelength range of 250–1050 nm while the moon was eclipsed by Jupiter (Porco et al., 2003). The 500 images were collected in three different datasets, during three different eclipses over a period of four days. Each dataset was collected over a period of two to three hours with individual images separated from each other by several seconds to a few minutes (Table 1). This resulted in the best temporal resolution to date of Io's hot spots seen from a spacecraft (Radebaugh et al., 2004). We report our analyses of these images for the brightest visible hot spots on Io at the time of observation.

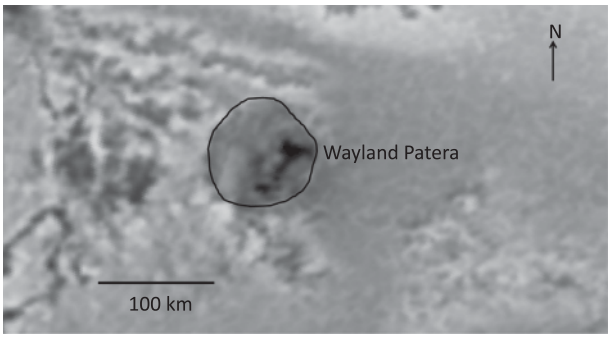

Fig. 1. Image showing Wayland Patera from the Galileo SSI basemap. Wayland Patera measures approximately 95 km across and is centered at 33°S, 225°W. The resolution is ~1 km/pixel.

2. Data and reduction procedures

2.1. Cassini and the raw data

Cassini was launched with an array of instruments aboard including the Imaging Science Subsystem (ISS), which contained the narrow-angle camera (NAC) used in this research. The double filter wheel system on the NAC allows images to be taken at wavelengths ranging from 250 nm out to 1050 nm (Porco et al., 2004). Images taken with two clear filters configured in place allows maximum transmission. These wavelengths are most sensitive to the hottest regions of the hot spots, which makes ISS ideal for constraining eruption temperatures between basaltic or ultramafic.

We used images of Io taken through a combination of the two clear filters (CL1 and CL2) and through the combination of one clear filter (CL1) and the infrared 4 filter (IR4) in our analysis because they gave the best signal-to-noise ratio for the hot spots. We refer to the double clear filter configuration as CL and the CL1-IR4 filter configuration as IR. The CL filter configuration has a wavelength range of 250–1050 nm while the IR configuration ranges from 875 nm to 1050 nm (Porco et al., 2004). NAC took ~500 total images of Io at a distance of closest approach of 9.72 million km, resulting in a spatial resolution of ~58 km/pixel (Porco et al., 2003). During the time of our observations, the spatial resolution varied from 60.5 km/pixel on December 29, 2000 to 61.3 km/pixel on January 1, 2001 (Geissler et al., 2004). Many of the 500 images were taken through other filters or did not contain at least one of our hot spots. Consequently, they were not used. Of the remaining images taken through the CL and the IR filter configurations, 69 were found to contain at least one of our hot spots.

We divided the 69 images into sequences according to which eclipse and day they were taken. Each sequence of images ranged in time from 2–3 h with exposure times between 2 and 12 s for each image depending on the day. As the NAC cycled through its filters, it captured a CL filter image or IR filter image every 12 min for eclipses 1 and 3 and every 8 min and 48 s for eclipse 2 (Table 1). Adjacent CL and IR images were spaced less than a minute apart for eclipses 1 and 3 and about 3 min apart for eclipse 2. This gave unprecedented temporal resolution for images taken by a spacecraft around Io, improving constraints on the rates at which volcanic thermal emission changes at individual hot spots. Short times between images and large flux uncertainties also made it possible to neglect a flux correction for the varying distance between Cassini and Io during imaging (see Section 4.1).

Better temporal resolution improves the chances of constraining eruption temperature and establishing the steadiness of the thermal emission. Short-lived events such as lava fountains occur on timescales of seconds and are good candidates for discriminating between basaltic or ultramafic eruption temperatures, which remains an open question regarding Io's lavas (Davies et al., 2011a). Observations at lower temporal resolution taken by the Galileo spacecraft, New Horizons, and ground-based telescopes have been used to study the temperature and variability of numerous hot spots on the surface (e.g., Davies et al., 2001; Howell and Lopes, 2007; McEwen et al., 1998a; Radebaugh et al., 2004; Spencer et al., 2007). Using techniques similar to these previous studies, we used the improved temporal resolution Cassini data to look at the temperature and variability of Pillan, Wayland Patera, and Loki Patera.

2.2. Data reduction procedures

The analysis began with the conversion of raw NAC images to files displayable in the Integrated Software for Imagers and

Table 1
Cassini eclipse observations.

Eclipse observation	Imaging date		SSC Lat	SSC Lon	Time between	
	Start time	End time			CL-IR	CL-CL
day364[a]	DEC 29, 2000 09:07:44.51	DEC 29, 2000 12:07:44.51	~0.5°N	300–324°W	48 s	12 min
day000	DEC 31, 2000 03:07:44.51	DEC 31, 2000 05:07:44.51	~0.2°S	286–302°W	3 min 13 s	8 min 48 s
day001	JAN 01, 2001 22:07:44.51	JAN 02, 2001 01:07:44.51	~0.8°S	280–305°W	48 s	12 min

[a] Each eclipse is given a name corresponding to the day in the year 2000 or 2001 when it began.

Spectrometers (ISIS) and the Image Reduction and Analysis Facility (IRAF). The raw NAC images were downloaded from archived Cassini data at the NASA Planetary Data System website. We converted the raw files into .cub files and .fits files for display in ISIS and IRAF, respectively.

Initial data reduction required the use of both ISIS and IRAF. We used ISIS to identify the hot spot and to find an average $n \times n$ box of pixel values or average data number (DN) around a given pixel or hot spot center as well as the x–y position of the hot spot. We then used IRAF and the x–y coordinates of the hot spots to find the flux or signal centered on the hot spot.

First, we subtracted the background contribution from each image. This was done to facilitate finding the fluxes using IRAF, to remove a 'prime signal' or hum present in the images (Fig. 2), and to aid in the error calculations of the hot spot signal. The source of this signal is unknown, but it causes the banding or hum at a frequency of ~2 Hz (Porco et al., 2004). The background subtraction required several steps for each image and involved creating an artificial background image with a separate background value for each row in the image.

We created an artificial background image by first using IRAF to find the midpoint value and standard deviation of all the pixels in each row. We used the midpoint values to make a file containing a value for each pixel in the image. We then used IRAF to create an artificial background image with every pixel in a given row in the image corresponding to the midpoint value found for that row. Finally, we subtracted this artificial background image from the corresponding original image using IRAF to produce a final image with the background removed.

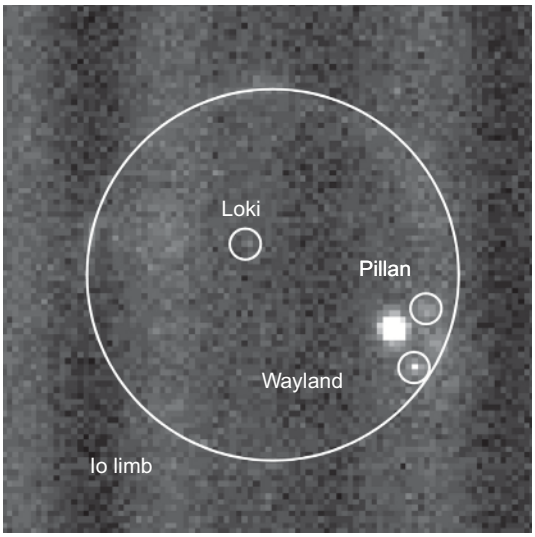

Fig. 2. Clear filter image (n1356774569) showing Pillan, Wayland Patera, Loki Patera and the limb of Io on December 29, 2000. Care had to be taken during analysis as the hot spots neared the limb to avoid unwanted contributions from auroral glows. The brightest hot spot just west of Pillan and Wayland Patera is Pele. Note the presence of a vertical prime signal or hum.

We found the flux from the hot spots in all of the images in both the CL and IR filters using the sky subtracted IRAF .fits files and the x–y coordinate files. We chose a circular aperture with radius of 1.5 pixels in IRAF to ensure we had adequate signal from the hot spot without including signal from nearby hot spots or auroral glows from Io. We then used these fluxes to find the color temperatures and uncertainties.

3. Color temperatures

3.1. Finding color temperatures

Color temperatures are found by taking observations in two different filters or wavelengths and comparing the ratio of the signals received by the NAC to the values obtained from the calibrated blackbody response curves of the NAC (see McEwen et al., 1998b; Radebaugh et al., 2004). The blackbody response curve from our two filters was found using the CL and IR filter transmission calibration files for the NAC. The transmission calibration files for each filter were produced by the Cassini ISS Team in collaboration with scientists at JPL while NAC was still on the ground and during transit. Tests were run to understand and calibrate the camera's response and the percentage of light that would be detected as a function of wavelength for each filter. A transmission calibration file was then produced for each filter that listed the percentage of light transmitted as a function of wavelength. We produced an expected blackbody response curve from these calibration files in order to find our color temperatures.

Color temperatures for Pillan, Wayland Patera, and Loki Patera were found by taking the ratio of the signal in the CL filter (250–1050 nm) to the IR filter (875–1050 nm) and comparing these values to the expected NAC blackbody response curve (Fig. 3). First, we paired each CL image with the corresponding IR image that was closest to it in time (see Table 1). The signals were found using IRAF as discussed in Section 2.2. We then divided the CL signal for one image with the signal from the neighboring IR image. We plotted the ratio for each image pair on the expected blackbody curve to find the corresponding color temperature. A typical plot is shown in Fig. 3 for Pillan. The error bars in the plot are $\sim 1\sigma$ and were found using the error analysis outlined in Appendix B. Each data point or ratio value on the curve is comprised of a CL and IR image chosen such that they are the closest images in time. Pairing images as closely as possible in time minimizes the errors introduced by time delays in image acquisition. Images captured simultaneously at two wavelengths would be preferred because changes in integration time of only 1 s can change the derived temperatures by as much as 255 K (Davies et al., 2011b). We discuss the implications of time delays in our images and the implied assumption of steady thermal hot spot emission below.

To find the lava compositions, we considered the highest and lowest color temperatures and associated uncertainties found for

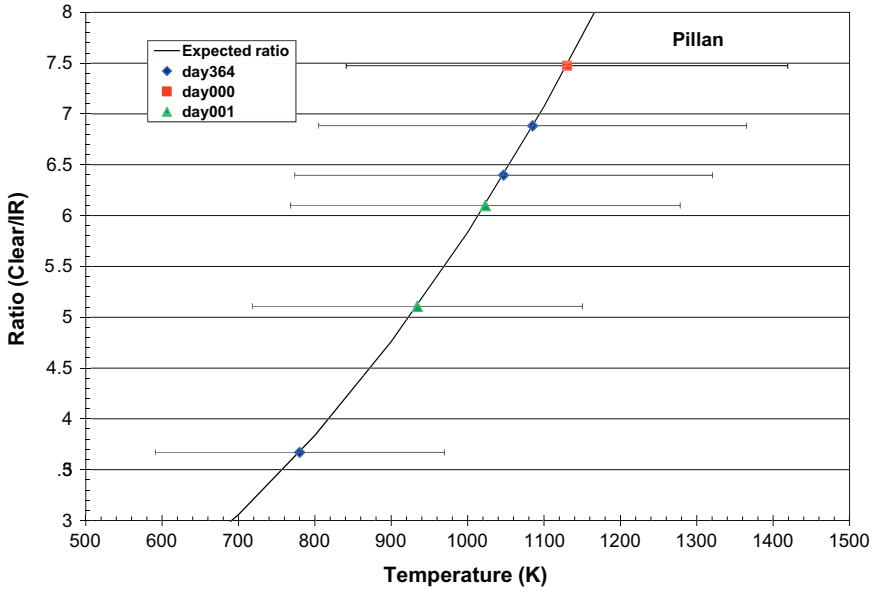

Fig. 3. Plot of ratios of emission from Pillan for CL and IR filters with the expected blackbody emission curve. The maximum color temperature is 1130 ± 289 K and the minimum color temperature is 780 ± 189 K. These temperatures suggest that the lava composition is basaltic. (For interpretation of the references to color in this figure legend, the reader is referred to the web version of this article.)

each hot spot. We then estimated the lava compositions at each hot spot by comparing the two color temperatures and uncertainties to temperatures of terrestrial lavas of known composition. Many of the IR images had a low signal from the hot spots, making interpretation of the temperatures a delicate process.

The most crucial element for interpreting the temperatures was the strength of the IR signal relative to the noise or IR signal uncertainty. The IR signal was at the limits of detectability and varied according to fluctuations in the background values. For example, low IR signal in some images contributed to an abnormally high temperature value because the background happened to be fluctuating higher at the time the image was taken. This led to a larger background subtraction at that point and thus a smaller IR signal and higher color temperature. Because of these fluctuations and the uncertainties involved, several of the temperatures we calculated were not considered in our analysis. Background subtraction during image processing also produced several IR images where the IR signal from the hot spot was negative. We also had two CL images with no corresponding IR image. Consequently, we found no temperature when the calculated IR signal was negative or when there was no IR image to pair with the CL image. This removed a potential four temperatures from Pillan, five from Wayland Patera, and two from Loki Patera.

We used a signal-to-noise ratio (S/N) analysis to determine which temperature points to keep and which points to remove. We divided the IR signal by the IR signal uncertainty to determine the IR S/N for each image and hot spot. This resulted in values ranging from 2.79 down to 0.40. Ideally, we would prefer S/N values of 10 or greater, but the quality of the IR images was not sufficient. Given the quality of the IR images and our range of S/N values, we decided on an IR S/N cutoff value of 1.5 or greater. A summary of this temperature analysis for Pillan, Wayland Patera, and Loki Patera is shown in Tables 2–4, respectively. We removed a total of 12 temperature values from Pillan, 6 from Wayland Patera, and 4 from Loki Patera using this analysis.

Finally, we removed an additional two temperatures and their corresponding electron fluxes for Loki Patera because they occurred near the beginning and the end of the eclipse. The increased light on the surface of Io as it emerged from behind Jupiter or before it was completely eclipsed caused an anomalous increase in the signal. This increase made the first and last electron fluxes too high on day364, and they were not considered in our analysis. Similarly, we removed the first electron flux value on day000 for Pillan because it occurred at the beginning of the eclipse.

We also recognize several factors that limit our goal of finding lava eruption temperatures, affect the outcome of our derived temperatures, and introduce uncertainties into the temperature analysis. One of the best candidates for deriving eruption temperatures on Io are lava fountains, which typically last a few seconds (Davies et al., 2011a). To definitively derive eruption temperatures and differentiate between basaltic or ultramafic lava composition, two criteria must be met when using multiple wavelength remotely-sensed data in the visible to near-IR. The spatial resolution must be high enough to separate the lava fountain from the surrounding material and the temporal resolution must be high enough to prevent errors associated with rapid cooling of the exposed lava (Davies et al., 2011a). Our spatial resolution (~61 km/pixel) does not meet the first requirement. Therefore, it is unlikely that our derived temperatures will be in the ultramafic range because the hottest erupting material gets averaged with the cooler surrounding material into a single pixel. Erupting lavas also cool very rapidly such that any time delays in acquiring the images introduces uncertainties in the derived temperatures by averaging the thermal emission and lowering the overall temperatures again. To accurately find the temperatures of the erupting lava fountains, the images must be acquired at least as fast as the process is occurring. The shortest amount of time between successive CL and IR images was 48 s, which does not meet the temporal resolution requirement. Thus, the likelihood of capturing the hottest temperatures was greatly diminished. Given these factors, the likelihood of deriving temperatures in the ultramafic range is not good. Our color temperatures should therefore be considered lower limits on the actual eruption temperatures of these lavas.

The large time delay between successive images also affects the derived temperatures and implies an assumption about the steadiness of the hot spots in order to extract meaningful temperatures. We assumed the hot spot emission was relatively constant between successive CL and IR images. If the hot spot emission

Table 2
Pillan – flux and calculated temperatures.

Hot spot Pillan	*T* K	*T* error K	CL flux counts/s	CL error counts/s	IR flux counts/s	IR error counts/s	IR S/N
day364	780[a]	189	19.94	3.54	5.43	2.19	2.48
	1298	337	21.60	3.66	2.16	1.82	1.19
	1085[a]	280	19.48	3.51	2.83	1.80	1.57
	1761	439	21.27	3.64	1.09	1.53	0.71
	2121	473	19.51	3.41	0.66	1.64	0.40
	1047[a]	273	18.99	3.46	2.98	1.88	1.58
	1892	459	20.36	3.57	0.89	1.50	0.59
day000	1684	364	23.40	4.15	1.32	1.45	0.91
	1036	288	12.47	3.40	1.99	1.66	1.20
	2097	415	18.34	3.81	0.64	1.49	0.43
	1130[a]	289	19.02	3.82	2.54	1.58	1.61
day001	1220	312	22.37	3.66	2.55	1.90	1.35
	1802	443	23.78	3.75	1.17	1.63	0.71
	1589	401	22.88	3.72	1.47	1.59	0.93
	1410	352	24.16	3.81	2.02	1.67	1.21
	1023[a]	255	20.10	3.52	3.30	1.85	1.78
	2008	477	22.77	3.72	0.87	1.49	0.58
	934[a]	216	22.08	3.64	4.32	1.99	2.17

[a] Indicates temperatures with IR flux S/N ratio greater than 1.5 used in the analysis.

Table 3
Wayland Patera – flux and calculated temperatures.

Hot spot Wayland Patera	*T* K	*T* error K	CL flux counts/s	CL error counts/s	IR flux counts/s	IR error counts/s	IR S/N
day364	1695	404	34.69	4.46	1.93	1.74	1.11
	2118	499	32.08	4.31	1.09	1.67	0.65
	1464	357	27.72	4.05	2.13	1.70	1.25
	2048	484	23.91	3.81	0.87	1.49	0.59
day000	1297[a]	289	28.93	4.47	2.89	1.61	1.79
	1116[a]	250	26.27	4.30	3.60	1.80	2.00
	1192[a]	272	25.00	4.20	2.99	1.62	1.85
day001	1751	434	24.83	3.78	1.29	1.64	0.78
	1473	391	16.58	3.24	1.26	1.72	0.73

[a] Indicates temperatures with IR flux S/N ratio greater than 1.5 used in the analysis.

Table 4
Loki Patera – flux and calculated temperatures.

Hot spot Loki Patera	*T* K	*T* error K	CL flux counts/s	CL error counts/s	IR flux counts/s	IR error counts/s	IR S/N
day364	1034[a]	186	16.00	1.54	2.57	0.97	2.65
	1387[a]	287	20.19	1.65	1.75	0.97	1.80
	1652	397	15.93	1.53	0.94	0.92	1.02
	1306[a]	300	14.16	1.47	1.40	0.92	1.52
	1541	344	18.29	1.58	1.26	0.87	1.44
	1538	345	18.62	1.61	1.28	0.91	1.42
day001	1692	368	23.67	1.69	1.32	0.91	1.46
	1017[a]	177	16.55	1.51	2.74	0.98	2.79
	1023[a]	197	13.77	1.44	2.26	0.92	2.45

[a] Indicates temperatures with IR flux S/N ratio greater than 1.5 used in the analysis.

changed rapidly during the time between images, it would introduce uncertainties in the derived temperatures. Analysis of terrestrial lava fountains revealed changes of up to 255 K in derived temperatures with a 1 s time delay between images (Davies et al., 2011b). We cannot say how these terrestrial results would change for a 48 s time delay or for Io itself so our temperature uncertainties do not explicitly include time delay errors. The errors introduced by such a time delay could be significant. However, the temperature averaging effect of our low spatial resolution images may ensure that our assumption is decent and that the time delays do not completely invalidate our derived temperatures.

3.2. Color temperatures and lava compositions

We found similar color temperatures and consequently lava compositions for all three hot spots. Pillan showed a variation of 350 K from a high of 1130 ± 289 K on day000 to a low of 780 ± 189 K on day364 (see Fig. 3 and Table 5). These temperatures are consistent with previous values found for Pillan (Davies et al., 2001; Keszthelyi et al., 2007; McEwen et al., 1998b) and indicate the presence of basaltic lava. Lava at the surface of Io cools rapidly suggesting that these temperatures underestimate the eruption temperature by as much as 200 K (Keszthelyi and McEwen,

Table 5
Hot spot color temperatures.

Hot spot	High T (K)	Low T (K)	Mean T (K)	Composition
Pillan	1130 ± 289	780 ± 189	962 ± 126	Basaltic
Wayland Patera	1297 ± 289	1116 ± 250	1193 ± 91	Basaltic
Loki Patera	1387 ± 287	1017 ± 177	1093 ± 179	Basaltic

1997). Even with the addition of 200 K, the temperatures are still consistent with a basaltic composition.

Wayland Patera's variation from high to low was 181 K with values of 1297 ± 289 K and 1116 ± 250 K, respectively. These temperatures also indicate the presence of basaltic lava. Wayland Patera had not been previously studied in two-filter observations at visible wavelengths, so this is the first measurement of the high temperature component for this hot spot (Geissler et al., 2004).

Loki Patera showed a maximum temperature of 1387 ± 287 K and a low temperature of 1017 ± 177 K, with a total range of 370 K. Within uncertainty, the low temperature result is consistent with the value of 878 K reported by Matson et al. (2006) for a two-temperature fit to Galileo NIMS data. This result comes from orbit G29 on December 28, 1999 and is the value closest to ours in time. The temperatures suggest basaltic lava composition and are consistent with a well-insulated, cooling lava surface such as a lava lake or thick flows with possible cracks revealing hotter material below. This is also consistent with results by Matson et al. (2006).

As discussed in Section 1, previous temperatures have been <1000 K and generally around 400–700 K (Davies, 2003; Howell and Lopes, 2007; McEwen et al., 1998a; Rathbun et al., 2002). Higher temperatures have been seen, but rarely (e.g. Blaney et al., 1995; Matson et al., 2006). Previous lower temperature derivations at Loki Patera are likely attributable to those observations being at longer wavelengths, which are more sensitive to the cooler surfaces. Thermal emission from vast expanses of warm lava crust can also overwhelm the thermal emission from the relatively small high-temperature areas and lower the derived temperatures. Our observations in the visible to near-IR are more sensitive to the high temperature component.

Other reasons for higher temperatures at Loki Patera may include a low emission angle or a change in the style of activity during the time of observation. A small angle of emission would enable the camera to see deeper into possible cracks on the lava surface and thus see higher temperatures. The emission angles for Loki Patera were low and ranged from ~30.4° to ~12.5°, comparable to the ~18° emission angle for Loki Patera seen by Galileo SSI on orbit E6 (McEwen et al., 1998a). McEwen et al. (1998a) inferred temperatures greater than 700 K for the hot spots given that SSI observed at wavelengths less than 1000 nm. Higher temperatures may also be the result of changing activity exposing more hot material such as foundering or overturning crust. With Cassini observing Loki Patera from almost directly overhead and observations in the visible to near-IR that are sensitive to hotter surfaces, we obtained higher temperatures than previously reported.

4. Variations in emission

In addition to finding color temperatures to infer lava composition, we used the images to track variations in intensity over time and emission angle for each hot spot. These variations allow us to determine the eruption style since different types of eruptions exhibit characteristic temporal behaviors (Davies et al., 2001). However, caution must be used in interpreting variations seen by short-wavelength data like Cassini ISS because these wavelengths are sensitive to the most variable and hottest areas of an eruption, which cool rapidly. This analysis used only the CL images, thus avoiding the uncertainties of the IR images with low S/N.

4.1. Spacecraft positions and fluxes

The positions of the spacecraft and hot spots are used to find the angle of emission as seen by Cassini. This angle changes throughout the eclipse as Io rotates and the spacecraft moves resulting in a change in emission from the hot spot. The way it changes relative to what we expect for a flat radiator can be used to determine the geometry of the hot spot in relation to the surrounding topography.

We also used the spacecraft distance and velocity to determine if a distance correction to the fluxes and temperatures was necessary. We assumed an initial Cassini-Io distance of 9.72 million km and a velocity of 11.6 km/s directly towards Io on December 30, 2000 (NASA-JPL, 2013). The largest time between successive CL and IR images was 3 min 13 s resulting in a change in intensity caused by distance of about 0.05%. Between successive pairs of images the largest time was 11 min 12 s, which resulted in a change in intensity of about 0.2%. The longest time from our first image to our last image was about 2 h or a change of about 1.7% in intensity. Our flux uncertainties averaged about 18% for Pillan and Wayland Patera and about 9% for Loki, a factor of at least 5 greater than the change in intensity caused by distance over the entire range of observations. Thus, we believe a distance correction can safely be ignored and any changes in flux are from the source and not caused by distance factors. Similarly, the change in temperature resulting from a change in distance over the largest time between successive CL and IR images is less than 0.03%. With temperature uncertainties ranging from about 20% to 25%, a distance correction for the temperatures can also safely be ignored.

We found the electron flux in electrons/s by obtaining the hot spot signal (DN) through the CL filter, dividing this signal by the integration time and multiplying by the gain (12 electrons/DN). Next, to correct for the rotation of Io and surrounding topography that might block the signal, we multiplied the electron flux by a multiplication factor to get a corrected electron flux. This multiplication factor is defined as

$$m = (1/\cos\theta)^x, \tag{1}$$

where θ is the emission angle and x is a factor which linearizes the corrected electron flux. As Io rotates, the hot spot visibility depends on whether topographical features block the hot spot emissions and on the changing emission angle. For a flat, constant radiator, we expect the emission to decrease by a factor of $\cos\theta$ or $x = 1$. A larger or smaller x factor gives us an idea of the geometry of the hot spot and surrounding area. An x factor >1 indicates a more rapid increase or decrease in electron flux than is expected for a flat radiator and a less rapid increase or decrease for an x factor <1. This technique also assumes a relatively constant hot spot flux. A hot spot experiencing short timescale variations such as lava fountaining cannot be corrected with this method.

The expectation for the value of the x factor from previous work (Radebaugh et al., 2004; Marchis et al., 2001) is a positive number greater than one. Marchis et al. (2001) suggested there was topography surrounding the Pele hot spot, which blocked the emission with increasing emission angle. This resulted in a value of x of 1.3 and thus a greater decrease in emission than expected for a flat radiator (Marchis et al., 2001). Studies of Cassini eclipse data for Pele by Radebaugh et al. (2004) resulted in an x factor of 1.6, indicating an even greater decrease in emission than expected.

We found the x factors by plotting the corrected electron flux as a function of CL filter emission angle starting with an x factor of one. We also plotted a linear fit to the corrected flux. Then, we

changed the x factor until the slope of the linear fit was closest to zero. We derived x factor values for Pillan and Wayland Patera, but because of large flux variations, x factors could not be found for Loki Patera.

4.2. Emission variations and eruption styles

Pillan's electron flux or total CL filter intensity appeared to decrease over the course of all three days (Fig. 4), although it did remain constant within our 1-sigma uncertainties. Significant change to a low value on day000 likely resulted from spuriously low pixel values in the vicinity of the hot spot. Thus the point was not considered in our analysis.

Despite being constant within uncertainty during each of the three days (Fig. 4), we calculated x factors to correct for the apparent decreasing emission with decreasing emission angle. We used all of the observations on day364 and day001, but we excluded the low point on day000. We found x factors of approximately 0.095, 3.13, and 0.36 for day364, day000, and day001, respectively. The day364 and day001 x factors indicate a less rapid decrease in emission with increasing emission angle. We expect a decrease in emission by a factor of $\cos\theta$ or $x = 1$ as Io rotates. The high value for day000 suggests that there may be some topography near the hot spot which blocks the emission and makes it drop more rapidly than expected. The mean intensity of Pillan calculated for each day of observations was also constant within uncertainty over the three day period, indicating a relatively constant volcanic output (Fig. 5).

The electron flux or total CL filter intensity for Wayland Patera decreased measurably during each of the three days (Fig. 6). We calculated x factors for all three days to see if the decrease in intensity was because of a decrease in emission or a decrease from increasing emission angle. For the calculations, we used the four observations on day364, but we only used the first four observations on day000 and the last four observations on day001 because the other measurements appeared to be errant points. We found x factors for day364, day000, and day001 of approximately 0.94, 3.31, and 3.82, respectively. These factors indicate that the emission decreased close to or a little less rapidly than the expected decrease by a factor of $\cos\theta$ for day364 and decreased much more rapidly on day000 and day001. Increased activity on day364 may have kept the emission from decreasing as rapidly as a flat rotator. The large x factors for day000 and day001 suggest some large topographic feature near the hot spot that may be blocking the emission and causing such a large decrease.

The mean intensity of Wayland Patera also decreased over timescales of tens of hours to several days (Fig. 5). It decreased from a mean of 349 ± 57 electrons/s on day364 to 174 ± 70 electrons/s on day001 over a period of around 61 h. These overall decreases in emission are indicative of a cooling lava flow or a cooling crust on a lava lake.

The electron flux or total CL filter intensity for Loki Patera both increased and decreased on day364, and it remained constant within uncertainty on day001 (Fig. 7). Intensity began day364 at a value of 192 ± 18 electrons/s and an emission angle of 13.9°. It increased rapidly to a value of 242 ± 20 electrons/s over a period of 12 min and then decreased to a value of 191 ± 18 electrons/s over the same time period. It remained relatively constant within uncertainty for the next 36 min before rising to a value of 219 ± 19 electrons/s in 12 min. These variations are indicative of an eruption that exposes areas at high temperatures such as those occurring on the surface of a lava lake or at the margins of a cooling lava flow. The intensity variations also indicate the brightening is a recurring event on a short timescale. These intensity variations may be caused by small lava fountains, cracks on a cooling lava crust opening and closing, foundering of crust on a lava lake, or break-up of a lava crust along the margins of a lava lake. The electron flux increased and decreased appropriately with emission angle (see next paragraph and Fig. 7), but the x factors were not found because of the rapidly varying fluxes. The mean intensity

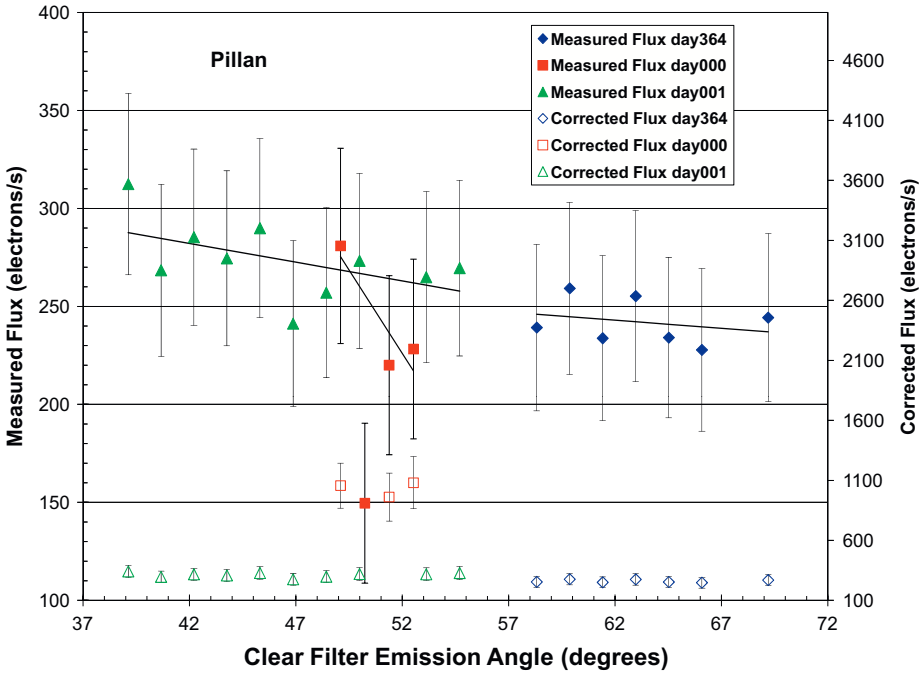

Fig. 4. Plot of electron flux versus emission angle for Pillan. Best fit lines are plotted on the measured fluxes with slopes of −0.83, −16.98, and −1.91 electrons/s/degree for day364, day000, and day001, respectively. The y-intercepts are 294.3, 1108.8, and 362.5 electrons/s for day364, day000, and day001, respectively. The corrected fluxes are plotted on the secondary y-axis. We found x factors of 0.095, 3.13, and 0.36 for day364, day000, and day001, respectively. *Note*: We used all points on day364 and day001, but we excluded the low point on day000.

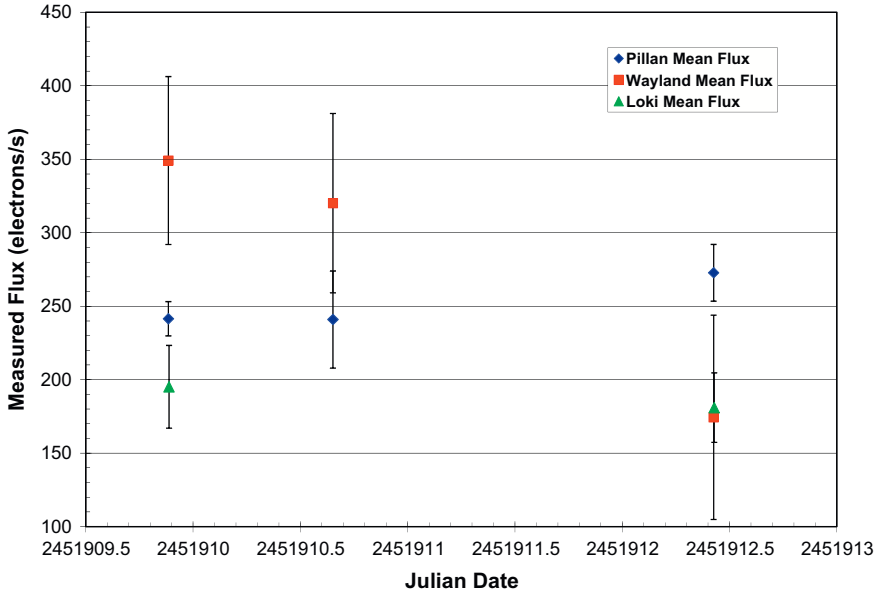

Fig. 5. Plot showing the day to day variations with time for all 3 hot spots. The mean fluxes were found for each day and plotted at the first time each day. Julian date provides the precise time the observation was taken and refers to the number of days elapsed since a specific date in history.

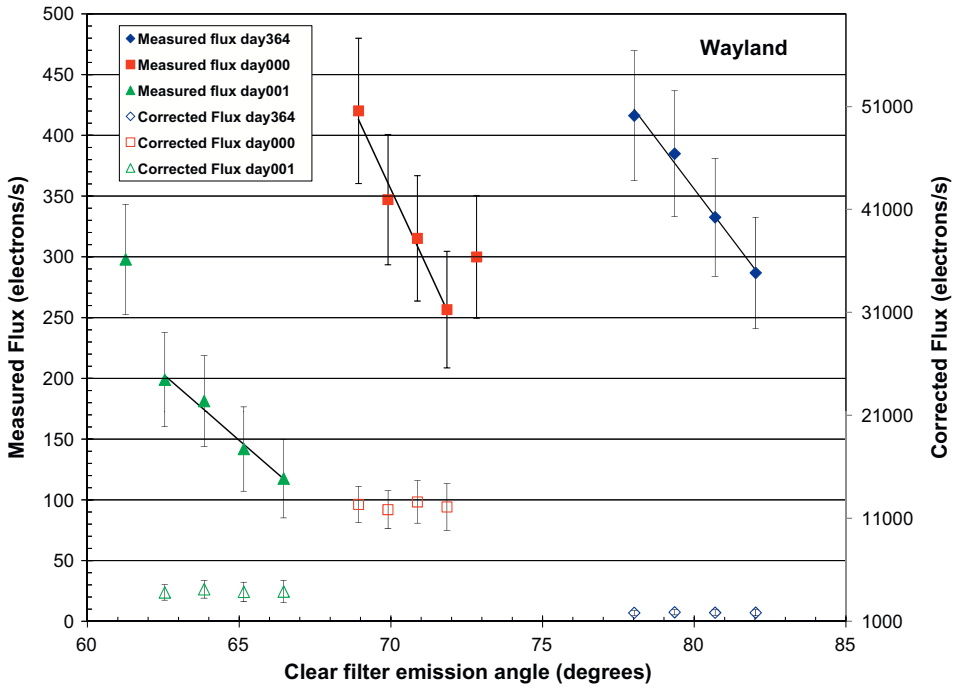

Fig. 6. Plot of electron flux versus emission angle for Wayland Patera. Best fit lines are plotted on the measured fluxes with slopes of −33.01, −53.80, and −21.73 electrons/s/degree for day364, day000, and day001, respectively. The *y*-intercepts are 2996.5, 4121.4, and 1561.7 electrons/s for day364, day000, and day001, respectively. The corrected fluxes are plotted on the secondary *y*-axis. We found *x* factors of 0.94, 3.31, and 3.82 for day364, day000, and day001, respectively. *Note*: We used all points on day364, the first 4 on day000, and the last 4 on day001 to find the *x* factors.

on timescales of tens of hours to several days for Loki Patera was constant within uncertainty (Fig. 5). This suggests a fairly constant overall output, indicative of a lava lake or large cooling lava flows.

Unlike the other two hot spots, the change in emission angle did not correspond to the change in time for the observations of Loki Patera. The Pillan and Wayland Patera plots for flux as functions of time and emission angle show the same variations. This is not so for Loki Patera. The reason for this is shown in Fig. 8. As Io rotated and Cassini moved, Loki Patera rotated into better view of the spacecraft and then out again. The emission angle decreased from 14.6° to a value of 12.5° and then back to 14.2° on day364.

5. Results and discussion

This analysis of Cassini observations of Io in eclipse by Jupiter during late 2000 and early 2001 provided results concerning temperatures and eruption styles of the three hot spots. We found

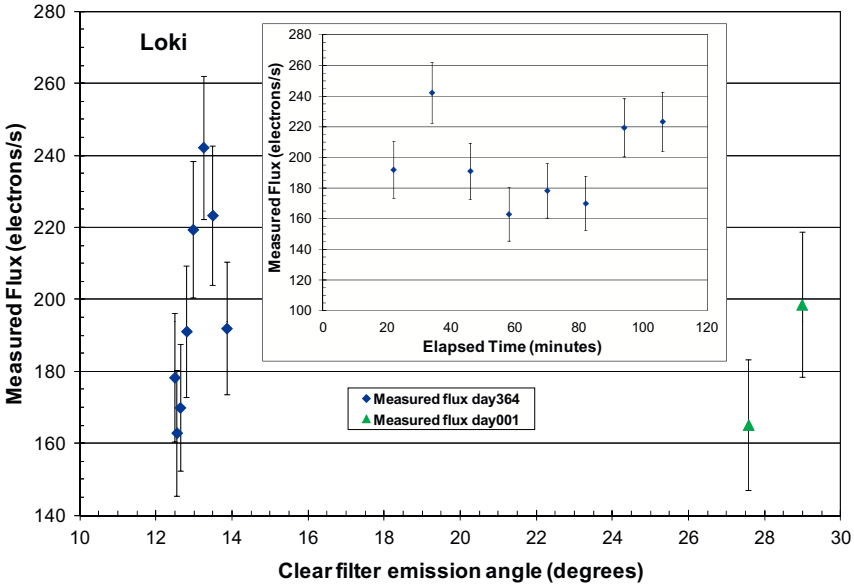

Fig. 7. Plot of electron flux versus emission angle for Loki Patera with electron flux versus time plotted on the inset because emission angles for Loki Patera decreased and then increased with time (see Fig. 8). The emission angle plot does not show how the flux changes with time. Corrected fluxes are not plotted because of the rapidly changing fluxes.

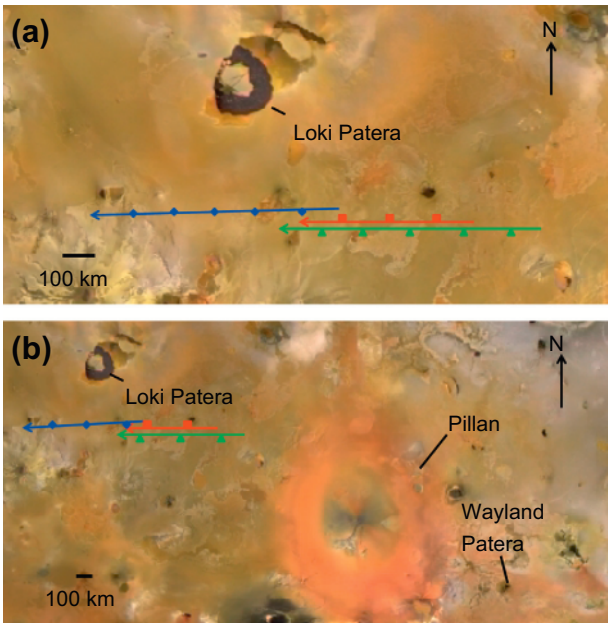

Fig. 8. Galileo images showing the region around our hot spots and the approximate subspacecraft position of Cassini on Io's surface. The lines and symbols correspond to the three eclipse days (day364 – blue diamond, day000 – red square, and day001 – green triangle). Pillan and Wayland Patera are below the lines, and as Io rotates and Cassini proceeds from right to left across the surface, the emission angle increases. The emission angle for Loki Patera decreases and then increases as Io rotates and Cassini moves. *Note*: The top image has a scale of ~5 km/pixel and the bottom has a scale of ~9 km/pixel. (For interpretation of the references to color in this figure legend, the reader is referred to the web version of this article.)

high and low color temperatures of 1130 ± 289 K and 780 ± 189 K for Pillan, 1297 ± 289 K and 1116 ± 250 K for Wayland Patera, and 1387 ± 287 K and 1017 ± 177 K for Loki Patera. These were all similar and are consistent with the presence of basaltic lava at all three. We cannot rule out the possibility of ultramafic lavas being present given the range at which the observations were taken and the likelihood of finding lavas at ultramafic temperatures when the images at different wavelengths were not taken simultaneously. Pillan showed constant thermal output within uncertainty over a period of 88 h. Corrections to the decrease in output with changing emission angle highlighted a possible drop in emissions in the middle of the observations (day000). We cannot say for certain if this decrease is real because the data are constant within uncertainty on this day, but such a drop would be consistent with the eruption disappearing behind a topographic obstacle. Wayland Patera's thermal output decreased gradually over 88 h, consistent with a cooling lava flow or lava lake at a period of low activity or quiescence. Corrections to the decrease in output with emission angle suggested Wayland Patera is in a depression surrounded by ridges, consistent with low-resolution images of Wayland Patera and characteristic of many hot spots contained within paterae on Io (Radebaugh et al., 2004). The most significant variations in emission over the course of the eclipse observations were observed at Loki Patera. The variations exceeded the changes resulting from changing emission angle. Overall, the observed temperatures and variations were consistent with previous characterizations and modeling of Loki Patera (e.g., Davies, 2003; Howell and Lopes, 2007; Matson et al., 2006; Rathbun et al., 2002) as a large, generally quiescent lava lake intermixed with periods of increased activity from overturning, crustal breakup or perhaps small lava fountains.

Acknowledgments

We would like to thank the Cassini Imaging Team for acquiring the data and to thank Julie Rathbun and Ashley Davies for their careful reviews, which greatly improved the manuscript. This project was supported by the NASA Cassini Data Analysis Program and Brigham Young University.

Appendix A. Data

See Tables A.6,A.7 and A.8.

Table A.6
Pillan – data

Hot spot Pillan	Image[a]	Time Julian date[b]	Emission angle degrees	T K	T error K	Measured flux electrons/s	Measured error electrons/s	Corrected flux electrons/s	Corrected error electrons/s
day364	73129	0.88461	58.32	780[c]	189	239.22	42.50	254.33	45.18
	73849	0.89294	59.86	1298	337	259.23	43.86	276.79	46.84
	74569	0.90128	61.42	1085[c]	280	233.78	42.08	250.76	45.14
	75289	0.90961	62.97	1761	439	255.29	43.62	275.17	47.02
	76009	0.91794	64.52	2121	473	234.11	40.94	253.66	44.36
	76729	0.92628	66.08	1047[c]	273	227.84	41.47	248.26	45.19
	78169	0.94294	69.19	1892	459	244.31	42.88	269.57	47.32
day000	26322	0.65767	49.10	1684	364	280.91	49.80	1057.18	187.41
	26850	0.66378	50.24	1036	288	149.64	40.80	606.02	165.22
	27378	0.66989	51.38	2097	415	220.04	45.68	961.97	199.72
	27906	0.67600	52.52	1130[c]	289	228.28	45.88	1080.92	217.23
day001	79071	0.42558	39.12	–[d]	–	312.44	46.30	342.51	50.76
	79791	0.43391	40.66	1220	312	268.50	43.88	296.74	48.50
	80511	0.44225	42.21	1802	443	285.36	45.01	318.11	50.18
	81231	0.45058	43.75	1589	401	274.56	44.66	308.87	50.24
	81951	0.45891	45.31	1410	352	289.95	45.69	329.35	51.90
	82671	0.46725	46.87	1023[c]	255	241.25	42.28	276.85	48.52
	83391	0.47558	48.43	–	–	257.04	43.40	298.17	50.34
	84111	0.48391	49.99	2008	477	273.28	44.60	320.66	52.34
	85551	0.50058	53.12	934[c]	216	264.94	43.67	318.74	52.54
	86271	0.50891	54.69	–	–	269.58	44.88	328.77	54.73

[a] Last 5 digits of the image number (day364 – n13567*****, day000 – n13569*****, day001 - n13570*****).
[b] Corresponds to the time for the CL filter image and equals 2451909.0, 2451910.0, and 2451912.0 plus the value given for day364, day000, and day001, respectively.
[c] Indicates temperatures with IR flux S/N ratio greater than 1.5 used in the analysis.
[d] Temperatures without a value occured when there was no corresponding IR image or when the IR image signal was found to be negative after image processing.

Appendix B. Error analysis

The error analysis was not a trivial task and required the use of traditional error propagation as well as a Monte Carlo technique to find the temperature uncertainties. The following sections describe the complete error analyses.

B.1. Signal errors

We computed the signal uncertainties using traditional error propagation techniques and an equation to account for both the error introduced by the source or hot spot and the error in the background. The signal error equation was

$$\sigma^2_{signal} = \sigma^2_{source} + n\sigma^2_{background}, \tag{B.1}$$

where n is the number of pixels in the aperture used to find the signal, which in this case was 7.343. The source error was computed using Poisson statistics such that

$$\sigma_{source} = \sqrt{N}, \tag{B.2}$$

where N is the number of counts from the source or the signal. The background error was calculated from the average standard deviation of the pixels in all of the rows in the image, σ_{pixel}, giving

$$\sigma_{background} = \sigma_{pixel}. \tag{B.3}$$

We found the standard deviation of the pixels in each of the 1024 rows in each image using *gstatistics* in IRAF and averaged them to find σ_{pixel}.

Table A.7
Wayland Patera – data.

Hot spot Wayland Patera	Image[a]	Time Julian date[b]	Emission angle degrees	T K	T error K	Measured flux electrons/s	Measured error electrons/s	Corrected flux electrons/s	Corrected error electrons/s
day364	73129	0.88461	78.02	1695	404	416.26	53.56	1831.79	235.67
	73849	0.89294	79.35	2118	499	384.96	51.75	1890.31	254.13
	74569	0.90128	80.68	1464	357	332.65	48.62	1850.78	270.52
	75289	0.90961	82.02	2048	484	286.87	45.74	1844.99	294.19
day000	25794	0.65155	68.93	–[d]	–	420.18	59.78	12368.79	1759.63
	26322	0.65767	69.90	1297[c]	289	347.16	53.64	11858.44	1832.27
	26850	0.66378	70.87	1116[c]	250	315.28	51.56	12604.08	2061.12
	27378	0.66989	71.85	–	–	256.65	48.03	12120.20	2268.08
	27906	0.67600	72.82	1192[c]	272	299.99	50.35	16909.50	2838.06
day001	79071	0.42558	61.26	1751	434	297.96	45.35	4869.33	741.20
	79791	0.43391	62.55	1473	391	198.98	38.84	3819.59	745.55
	80511	0.44225	63.84	–	–	181.30	37.44	4129.94	852.83
	81231	0.45058	65.15	–	–	141.88	34.62	3878.60	946.42
	81951	0.45891	66.46	–	–	117.55	32.45	3903.96	1077.68

[a] Last 5 digits of the image number (day364 – n13567*****, day000 – n13569*****, day001 – n13570*****).
[b] Corresponds to the time for the CL filter image and equals 2451909.0, 2451910.0, and 2451912.0 plus the value given for day364, day000, and day001, respectively.
[c] Indicates temperatures with IR flux S/N ratio greater than 1.5 used in the analysis.
[d] Temperatures without a value occured when there was no corresponding IR image or when the IR image signal was found to be negative after image processing.

Table A.8
Loki Patera – data.

Hot spot Loki Patera	Image[a]	Time Julian date[b]	Emission angle degrees	*T* K	*T* error K	Measured flux electrons/s	Measured error electrons/s	Corrected flux electrons/s	Corrected error electrons/s
day364	74089	0.89561	13.85	1034[c]	186	191.99	18.42	–[d]	–
	74809	0.90394	13.24	1387[c]	287	242.28	19.84	–	–
	75529	0.91227	12.80	1652	397	191.16	18.31	–	–
	76249	0.92061	12.54	–[e]	–	162.94	17.40	–	–
	76969	0.92894	12.48	–	–	178.34	17.87	–	–
	77689	0.93727	12.63	1306[c]	300	169.97	17.65	–	–
	78409	0.94561	12.97	1541	344	219.45	19.01	–	–
	79129	0.95394	13.48	1538	345	223.40	19.32	–	–
day001	79311	0.42824	30.40	1692	368	283.99	20.23	–	–
	80031	0.43658	28.97	1017[c]	177	198.60	18.13	–	–
	80751	0.44491	27.57	1023[c]	197	165.21	17.23	–	–

[a] Last 5 digits of the image number (day364 – n13567*****, day001 – n13570*****).
[b] Corresponds to the time for the CL filter image and equals 2451909.0 and 2451912.0 plus the value given for day364 and day001, respectively.
[c] Indicates temperatures with IR flux S/N ratio greater than 1.5 used in the analysis.
[d] Corrected fluxes were not found because of the rapidly varying fluxes.
[e] Temperatures without a value occured when there was no corresponding IR image or when the IR image signal was found to be negative after image processing.

B.2. Monte Carlo temperature errors

We used a Monte Carlo simulation to find the uncertainties in the temperatures. The program *temphist.f* (Stephens, 2010) uses the CL and IR signals and associated uncertainties to find a possible range of temperatures and the standard deviation. It does this by taking the first CL and IR signals from an input file and assuming a gaussian error distribution. It calculates new CL and IR signal values, finds the CL/IR signal ratio, and calculates a new temperature. The program runs this process a million times to get a gaussian distribution of a million temperature values. It finds the mean temperature value from this distribution and the 1-sigma deviation and returns them as the final temperature and uncertainty. The process is repeated for each pair of CL and IR signals in the input file, and the results are written to an output file. In our analysis, we used our previously calculated temperature values and the uncertainties given by *temphist.f*.

B.3. Electron flux errors

We calculated the electron flux uncertainties using the signal errors as described in Appendix B.1. The measured electron fluxes were given by

$$F_m = S_{Clear} G, \tag{B.4}$$

where S_{Clear} is the CL filter hot spot signal divided by the exposure time and G is the gain of 12 electrons/DN. The related errors were found using

$$\sigma_{F_m} = G\sigma_{S_{Clear}}. \tag{B.5}$$

We used the calculated uncertainties for the plus and minus of the error bars as seen in Fig. 6.

References

Blaney, D.L., Johnson, T.V., Matson, D.L., Veeder, G.J., 1995. Volcanic eruptions on Io: Heat flow, resurfacing, and lava composition. Icarus 113, 220–225.

Davies, A.G., 1996. Io's volcanism: Thermo-physical models of silicate lava compared with observations of thermal emission. Icarus 124, 45–61.

Davies, A.G., 2003. Temperature, age and crust thickness distributions of Loki patera on Io from Galileo NIMS data: Implications for resurfacing mechanism. Geophys. Res. Lett. 30, 2133–2136.

Davies, A.G., Keszthelyi, L., McEwen, A.S., 2011a. Estimating eruption temperature from thermal emission spectra of lava fountain activity in the Erta'Ale (Ethiopia) volcano lava lake – Implications for observing Io's volcanoes. Geophys. Res. Lett. 38, L21308. http://dx.doi.org/10.1029/2011GL049418.

Davies, A.G., Keszthelyi, L.P., McEwen, A.S., 2011b. Erta'Ale (Ethiopia) lava lake thermal emission variability – What we need to measure to answer the biggest open question about Io's lavas. Lunar Planet. Sci. Conf. 42.

Davies, A.G. et al., 2001. Thermal signature, eruption style, and eruption evolution at Pele and Pillan on Io. J. Geophys. Res. 106, 33079–33103.

Davies, A.G., Veeder, G.J., Matson, D.L., Johnson, T.V., 2012. Io: Charting thermal emission variability with the Galileo NIMS Io Thermal Emission Database (NITED): Loki Patera. Geophys. Res. Lett. 39, L01201. http://dx.doi.org/10.1029/2011GL049999.

Geissler, P.E., McEwen, A., Porco, C., Strobel, D., Saur, J., Ajello, J., West, R., 2004. Cassini observations of Io's visible aurorae. Icarus 172, 127–140.

Howell, R.R., Lopes, R.M.C., 2007. The nature of the volcanic activity at Loki: Insights from Galileo NIMS and PPR data. Icarus 186, 448–461.

Keszthelyi, L., Jaeger, W., Millazo, M., Radebaugh, J., Davies, A.G., Mitchell, K.L., 2007. New estimates for Io eruption temperatures: Implications for the interior. Icarus 192, 491–502.

Keszthelyi, L., McEwen, A.S., 1997. Thermal models for basaltic volcanism on Io. Geophys. Res. Lett. 24, 2463–2466.

Keszthelyi, L. et al., 2001. Imaging of volcanic activity on Jupiter's moon Io by Galileo during the Galileo Europa Mission and the Galileo Millennium Mission. J. Geophys. Res. 106, 33025–33052.

Lopes, R.M.C. et al., 2001. Io in the near infrared: Near-Infrared Mapping Spectrometer (NIMS) results from the Galileo flybys in 1999 and 2000. J. Geophys. Res. 106, 33053–33078.

Marchis, F., dePater, I., Davies, A.G., Roe, H.G., Fusco, T., Mignant, D.L., Descamps, P., Macintosh, B.A., Prange, R., 2002. High-resolution Keck adaptive optics imaging of violent volcanic activity on Io. Icarus 160, 124–131.

Marchis, F., Prange, R., Fusco, T., 2001. A survey of Io's volcanism by adaptive optics observations in the 3.8 μm thermal band (1996–1999). J. Geophys. Res. 106, 33141–33159.

Matson, D.L., Blaney, D.L., Johnson, T.V., Veeder, G.J., Davies, A.G., 1998. Io and the early Earth. Lunar Planet. Sci. Conf. XXIX. Abstract 1650.

Matson, D.L., Davies, A.G., Veeder, G.J., Rathbun, J.A., Johnson, T.V., Castillo, J.C., 2006. Io: Loki Patera as a magma sea. J. Geophys. Res. (Planets) 111, E09002. http://dx.doi.org/10.1029/2006JE002703.

McEwen, A.S., Keszthelyi, L., Geissler, P., Simonelli, D.P., Carr, M.H., Johnson, T.V., Klaasen, K.P., Breneman, H.H., Jones, T.J., Kaufman, J.M., Magee, K.P., Senske, D.A., Belton, M.J.S., Schubert, G., 1998a. Active volcanism on Io as seen by Galileo SSI. Icarus 135, 181–219.

McEwen, A.S. et al., 1998b. High-temperature silicate volcanism on Jupiter's moon Io. Science 281, 87–90.

NASA-JPL, 2013. Cassini Solstice Mission: Frequently asked Questions – General Information. saturn.jpl.nasa.gov/faq/FAQgeneral (accessed 01.03.13).

Peale, S.J., Cassen, P., Reynolds, R.T., 1979. Melting of Io by tidal dissipation. Science 203, 892–894.

Pearl, J. et al., 1979. Identification of gaseous SO_2 and new upper limits for other gases. Nature 280, 755–758.

Porco, C.C. et al., 2003. Cassini imaging of Jupiter's atmosphere, satellites, and rings. Science 299, 1541–1547.

Porco, C.C. et al., 2004. Cassini imaging science: Instrument characteristics and anticipated scientific investigations at Saturn. Space Sci. Rev. 115, 363–497.

Radebaugh, J., McEwen, A.S., Milazzo, M.P., Keszthelyi, L.P., Davies, A.G., Turtle, E.P., Dawson, D.D., 2004. Observations and temperatures of Io's Pele patera from Cassini and Galileo spacecraft images. Icarus 169, 65–79.

Rathbun, J.A., Spencer, J.R., Davies, A.G., Howell, R.R., Wilson, L., 2002. Loki, Io: A periodic volcano. Geophys. Res. Lett. 29, 1443. http://dx.doi.org/10.1029/2002GL014747.

Rathbun, J.A., Spencer, J.R., Tamppari, L.K., Martin, T.Z., Barnard, L., Travis, L.D., 2004. Mapping of Io's thermal radiation by the Galileo photopolarimeter–radiometer (PPR) instrument. Icarus 169, 127–139.

Spencer, J.R., Jessup, K.L., McGrath, M.A., Ballester, G.E., Yelle, R., 2000. Discovery of gaseous S_2 in Io's pele plume. Science 288, 1208–1210.

Spencer, J.R. et al., 2002. A new determination of Io's heat flow using diurnal heat balance constraints. Lunar Planet. Sci. Conf. XXXIII. Abstract 1831.
Spencer, J.R. et al., 1997. A history of high-temperature Io volcanism: February 1995 to May 1997. Geophys. Res. Lett. 24, 2451–2454.
Spencer, J.R. et al., 2007. Io volcanism seen by New Horizons: A major eruption of the Tvashtar volcano. Science 318, 240–243.
Stephens, D.C., 2010. Temphist.f. Computer Program.
Veeder, G.J., Davies, A.G., Williams, D.A., Matson, D.L., Johnson, T.V., Radebaugh, J., 2011. Io: Heat flow from dark paterae. Icarus 212, 236–261.
Vlaar, N.J., van Keken, P.E., van den Berg, A.P., 1994. Cooling of the Earth in the Archaean: Consequences of pressure-release melting in a hotter mantle. Earth Planet. Sci. Lett. 121, 1–18.
Williams, D.A., Greeley, R., Lopes, R.M.C., Davies, A.G., 2001. Evaluation of sulfur flow emplacement on Io from Galileo data and numerical modeling. J. Geophys. Res. 106, 33161–33174.
Williams, D.A. et al., 2002. Geologic mapping of the Chaac-Camaxtli region of Io from Galileo imaging data. J. Geophys. Res. 107 (E9), 5068. http://dx.doi.org/10.1029/2001JE001821.